Performance of Beamforming for a Handheld Device in Measured 21.5 GHz Indoor Channels

Nielsen, Jesper Ødum; Pedersen, Gert Frølund

Published in:
I E E E Transactions on Antennas and Propagation

DOI (link to publication from Publisher):
10.1109/TAP.2022.3161567

Publication date:
2022

Document Version
Accepted author manuscript, peer reviewed version

Performance of Beamforming for a Handheld Device in Measured 21.5 GHz Indoor Channels

Jesper Ødum Nielsen, Gert Frølund Pedersen

***Abstract*—This paper presents an evaluation of the performance of two different approaches for beamforming (BF) in a fifth generation (5G) handset, based on measured channels from a dual-polarized transmitter (Tx) to a mockup handset with a 7-element receiver (Rx) array. The measurements at 21.5 GHz are including both small-scale and large-scale channel changes and were conducted for different users holding the mockup at different locations in an indoor corridor environment. The unique measurements enable novel results based on statistics of the power achieved with BF, using channel state information (CSI) measured at a 90 Hz rate, and both when using beam scanning (BS) and the equal gain combining (EGC) reference case. For the case of ideal CSI knowledge, BF gains of up to about 18 dB were found. However, when the density of the angle scanning grid is reduced and the CSI is delayed to realistic values, the average performance decreases by 8 dB. More results are given in the paper.**

***Index Terms*—Cellular communications, channel sounding, mm-wave propagation, beamforming, user impact, radio propagation measurements**

I. Introduction

Fifth generation (5G) networks are expected to provide a significantly higher network capacity than previous generations [1]. One of the ways to achieve the higher capacity comes from the introduction of new bands at frequencies above those typically used in fourth generation (4G) networks. The 5G new radio (NR) specifications define the frequency range 2 (FR2) to cover the band 24.25–52.6 GHz [2], where channels below 30 GHz are of particular interest, since propagation losses are expected to be lowest generally. Unless otherwise specified, in the following the term *mmwave* band will be used loosely to mean frequency bands within FR2.

Although mmwave bands have been used previously, *e.g.*, for point-to-point links and wireless local area networks (WLANs), mmwave bands have only in the last about 10 years been considered for the link between the mobile station and the base station in cellular networks [3]. The properties of the mmwave radio channels are different than those of the legacy bands below 3 GHz, and the new channel has been the subject for a large number of publications. Examples of early works are [4]–[6], based on mechanically steered directive antennas and focusing on general feasibility of mmwave bands for cellular systems, at least for outdoor scenarios. Building penetration losses at 28 GHz are found to be large in [7], concluding that outdoor-to-indoor penetration will be difficult in many cases due to large losses. Results from using a 5G radio access prototype to measure 4×4 multiple input multiple output (MIMO) channels at 15 GHz were reported in [8]. The system allowed measurements while moving along routes in micro-cellular setups, for results on path loss, penetration loss and beamforming (BF) gain.

More recently, Lee *et al* [9] reports results based on outdoor to indoor (O2I) measurements at 32 GHz, with different transmitter incidence angles. The delay and angular spreads are found not to have dependency on the incidence angle. Based on O2I measurements at 32 GHz in both a traditional building and a thermally-efficient building, the work [10] finds that angular and delay dispersion statistics do not show any significant differences between the two building measurements. Outdoor measurements made at 28 GHz and 39 GHz bands are presented in [11], and used for characterizing directional and omni-directional path loss, as well as fading characterization and the influence of vegetation on delay and angular spreads. In [12] wide-sense stationarity is investigated using 28 GHz measurements in an outdoor expressway scenario, where stationary distances are found to be 6–23 wavelengths. Based on 28 GHz measurements in a library setting, models for power angular-delay profiles and large-scale path losses are presented in [13] for distances 10–50 m in both line of sight (LOS) and non-line of sight (NLOS) cases. The work in [14] presents measurements around 60 GHz in a variety of indoor environments in LOS and NLOS, as well as for both vertical and horizontal polarization. From the measurements level crossing rate and average fading duration statistics are estimated and fading models are tested.

Important use cases for mobile communication involves user equipment (UE) such as smartphones, *e.g.*, held in the user's hand or carried on the body. The term *handset* is used in the following for this type of UE. Using mmwave for handsets necessitates the use of high-gain antennas [15], which furthermore must be electronically steerable, since the orientation of the handset in the environment is generally unknown *a priori* and may change during the lifetime of the link. In addition, the propagation channel is typically also unknown and changing, and may have several propagation paths. It is therefore important that the high-gain antenna system of a handset can adapt its beams optimally. A convenient metric of an antenna's capability in this aspect is the coverage efficiency, based on the total scan pattern [16], [17], which is the gain the antenna achieves for each possible direction. For simplicity, the metric only considers single directions.

Another aspect is how the handset determines in which direction the high-gain antenna should aim. In the 3GPP specifications for 5G [18] this has been divided into the *initial access* phase, when the handset first connects to the

J. Ø. Nielsen, G. F. Pedersen are with the APMS section, Dept. of Electronic Systems, Technical Faculty of IT and Design, Aalborg University, Denmark.

Published in *IEEE Transactions on Antennas and Propagation*, Vol. 70, No. 7, p. 5725–5735, July 2022. DOI: 10.1109/TAP.2022.3161567.

network and must consider all possible directions, and the *tracking* phase when the handset already has a connection and might assume gradual changes to the existing direction [19]. To help initial access the network broadcasts SS/PBSCH blocks [20] allowing initial access and estimation of link quality. Depending on configuration, the SS/PBSCH blocks are broadcast every 5–160 ms [19]. The tracking phase can be based on the CSI-RS reference signals [18] which may be transmitted with intervals of 5–640 slots, corresponding to 1.17–149 ms for the lowest sub-carrier spacing and 0.292–37.3 ms for the highest sub-carrier spacing. The performance of the network in terms of, *e.g.*, adaptability to channel changes and control overhead, depends highly on the exact configuration of the network and choice of algorithms [21].

Fitting an adaptive high-gain antenna into the limited volume available in a typical smartphone-like device is challenging and subject of research [22]. The work in [23] is an example, presenting a 4-element dual-polarized phased array for an about 74 mm $\times$ 143 mm size handset achieving gains of 4.5–8 dBi within scanning angles -54° to 44° at 29 GHz. Another design example is [24] presenting a 28 GHz 2×4 series chained patch array fitting in a 70 mm $\times$ 142 mm $\times$ 8 mm handset with about 13 dB gain for scanning angles $\pm30^\circ$ (yz-plane) or, operated as two 1×4 phased arrays with about 10 dB gain and $\pm45^\circ$ scanning angles (xy-plane). A hybrid solution for better spherical coverage is suggested in [25], consisting of two horizontally polarized 4-element antenna in package (AiP) arrays with maximum gain of 9.2 dBi, placed at two corners of a handset in addition to an optically transparent 16 element array with a gain of 12.8 dBi.

An early 28 GHz 5G prototype handset with two 16-element arrays is shown in [26], with BF achieved using phase shifters and with other radio frequency (RF) parts located outside of the handset. The handset was tested in indoor LOS conditions, where the strongest beam directions were searched for. Another similar early work was presented in [15] where a 32-element uniform planar array was fit in a handset prototype, allowing adaptive BF with scanning for the best beams within 45 ms.

The importance of using the optimum beam directions is quantified in [27]. Based on propagation measurements at 28 and 38 GHz in indoor rail and airport terminals, the work investigates the power loss due to misalignment of a fixed Tx antenna and a receiver (Rx) horn antenna which was mechanically rotated. Using a simple model, it was found that a 3 dB loss was incurred by an antenna misalignment of just 4.3° for LOS and 6° for NLOS. The work [28] describes a testbed at 28 GHz for testing of the tracking capabilities of BF antenna systems, allowing testing of beam tracking algorithms via emulation of trajectories of vehicular devices, such as unmanned aerial vehicles (UAVs), cars, and trains.

The effect of the user's body on the received power is investigated in [29], using ray-tracing simulation of 15 GHz and 28 GHz outdoor urban mobile channels and measured radiation patterns of the different prototype antennas. The work finds large user shadowing losses of 30–35 dB and that the received signal quality is highly dependent on the relative positions of the handset and user.

Only a few prior publications present evaluation of the performance of BF in actual propagation channels involving handset antennas. Works based on measured channels typically focus on characterizing or modeling the propagation channel, trying to exclude effects of the antennas used for measurements. The impact of the handset antennas are included by using radiation patterns, as in [29]. However, with this approach it is difficult to include dynamic blocking and scattering by the user holding the device. This is possible with prototypes, such as in [15], [26], but here only few studies were done and is limited to the algorithms implemented in the prototypes.

The current work investigates BF in a mobile handset operating at 21.5 GHz, based on propagation measurements using a mockup handset equipped with a 7-element array. A series of measurements were carried out in an indoor corridor environment, each with a user holding the mockup while moving in the channel. During the movements, channel snapshots for all antenna elements were obtained at a rate of 90 Hz. These unique measurements allow for a performance analysis of different BF approaches for realistically changing channels, something which is missing in the current literature.

BF is obtained by using a weighted sum of the outputs of the individual elements in the antenna array. Depending on the choice of weights, different properties are achieved. One approach to finding an optimum set of weights is to assume arrival of a single plane wave from a number of specific directions, and determine the direction resulting in the largest Rx power. In this work, this approach is referred to as beam scanning (BS). Since waves may arrive from several directions at the same time, the BS approach may not be the best. Assuming knowledge of the channel coefficient phase for all individual antenna branches, equal gain combining (EGC) can be used instead, which is optimum for multiple waves and may be considered a reference.

In this work both the EGC and BS approaches are investigated using statistics of the Rx power obtained with the beamformer adapted to the instantaneous channel state information (CSI). The novel contributions are within the following main topics.

- BF gain performance for actual propagation scenarios, both in LOS and NLOS, and including the influence of different handset users.
- Impact of angular scanning grid density on performance. Using a coarse grid is desirable in order to reduce BS time, but may result in non-optimal directions.
- Impact of using delayed CSI on performance. Ideally the BF should be applied to the same channel state as was observed when determining the BF weights. In practice there will be certain delay which will cause a performance degradation.

The rest of the paper is structured with the measurements described in Section II, followed by the used combining methods in Section III. The coverage efficiency of the mockup handset is evaluated in Section IV. Details of the measurement processing are given in Section V and the results are discussed in Section VI, followed by conclusions in Section VII.

Published in *IEEE Transactions on Antennas and Propagation*, Vol. 70, No. 7, p. 5725–5735, July 2022. DOI: 10.1109/TAP.2022.3161567.

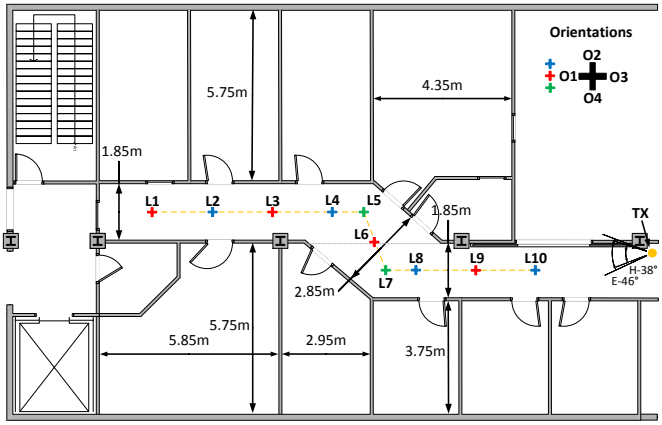

Fig. 1. Floorplan with measurement locations. © 2017 IEEE. Reprinted, with permission, from [30].

Fig. 2. Free space measurements in the corridor.

II. Measurements

The measurements analyzed in this work are from an indoor corridor environment where the fixed Tx antenna was mounted at 2.05 m above the floor and an array of Rx antennas in a mockup handset was held by a user. The measurements were previously described in [30], with only a summary given here. More details about the channel sounding system are available in [31]. In the setup used for the current work, two Tx channels are measured simultaneously, with Tx1 and Tx2 connected to the vertical and horizontal ports, respectively, of the dual-polarized Tx horn antenna. A single Rx branch of the sounder is connected to the handset mockup where a switch allows measurements from 7 Rx antenna elements. The sounding was carried out with a bandwidth of about 200 MHz, centered at 21.5 GHz. Obtaining the channel impulse responses (CIRs) for all the 2×7 channel combinations is completed in about 573 μs; one such set of CIRs is denoted a channel *snapshot* in the following. The snapshots are obtained at rate of 90 Hz, where a *measurement* designates a series of $R = 1800$ snapshots. The snapshot rate is high enough to capture many samples of changes in the channel due to user movements, as described below, but not sufficient for complete channel reconstruction from the samples. The latter is not needed for the current work.

The overall measurement campaign includes a number of scenarios of which only some are used and described in the current work. Note that these measurements were not included in the description given in [30].

For a given measurement a user holds the mockup in front while standing at a specified location in the corridor. While maintaining the hand grip and arm posture, the user rotates slowly clockwise, for one full 360° revolution during the 20 s long measurement. Due to the rotation, a fading and rather dynamic channel is expected, since the direction towards the Tx and major signal paths change and any blocking by the user will also change.

As shown in Fig. 1, the user locations L1, L2, ..., L10 are distributed in the corridor with L1 furthest away, about 17 m from the Tx along the corridor, and the L10 closest with about 3.6 m to the Tx. Between L4 and L7 there is a bend in the corridor, so that L1 to L6 are in NLOS while L7 to L10 are in LOS. About 1.7 m from L1 the corridor ends in a door, which was closed during measurements.

Measurements were carried out with 5 volunteer persons holding the handset, where four of the persons repeated L5 and L7 three times, and one person repeated L5 and L7 10 times. However, some of the measurements were subsequently discarded, e.g., due to too low power or errors during the measurements. In addition, measurements were made with the handset mounted at an angle of 60° from vertical on a expanded polystyrene foam (EPS) column, with no user nearby, as described in [30]. These measurements, labeled as *free space* in the following, were made at all locations, with three repetitions at L5 and L7. Fig. 2 shows the setup for free space measurements at L7.

On the handset mockup, the $K = 7$ antenna elements form a linear array with about $\lambda/2$ element spacing at 21.5 GHz. The frequency was chosen considering the 5G candidate bands when the antenna was designed [32], and not far from the 24–27 GHz band later assigned for 5G. The 7-element array approximately fits the width of a typical smartphone. The array is implemented on a 110 mm × 55 mm printed circuit board (PCB) and is located near the top end, as shown in Fig. 3(a). The PCB is mounted on the switch connected to the individual elements, with the switch also serving as the main body of the mockup. The PCB is mounted so that the array has a clearance of 40 mm from the switch top-end on the back. Details about the array design and the mockup are given in [33] and [30] where it is noted that array offers good efficiency, good impedance matching level and low mutual coupling. During the measurements the mockup is held by a user, so that the array is facing the user at an angle of about 60°. Each patch antenna element has a 5 dBi directive pattern towards the user. For the current work, the radiation patterns of all the elements have been measured in an anechoic room. The patterns were measured with the mockup (including switch and cables), as during the free space measurements. The setup is

Published in *IEEE Transactions on Antennas and Propagation*, Vol. 70, No. 7, p. 5725–5735, July 2022. DOI: 10.1109/TAP.2022.3161567.

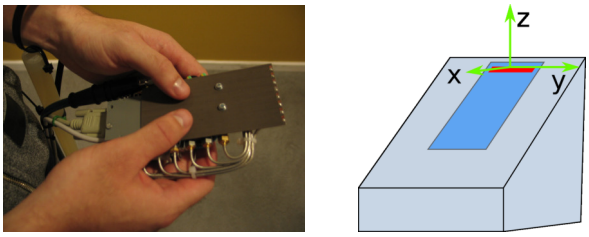

(a) (b)

Fig. 3. (a) Mockup handset held by a user. (b) Sketch of the anechoic room antenna measurement setup, with the mockup shown in dark blue and the antenna elements are in the red area. The mockup was fixed at an angle of 60° to a block of EPS. The coordinate system is centered at the array and with the y-axis along the array.

sketched in Fig. 3(b).

III. Combining Methods

Typically phased arrays are considered as a number of identical elements arranged in an array with identical spacing, allowing the effects of element patterns and array structure to be studied separately. In this work a slightly different view is applied, where the individual elements are measured as located in the array using the same reference point. Thus, the measured complex amplitudes include differences caused by both the element patterns and their location in the array.

This section describes the two combining methods that are used in this work from an Rx point of view, although the weighting also can be applied for Tx, assuming channel reciprocity. A narrowband system is considered so that a model of the received signal $y_k(r)$ at one element is

$$\begin{aligned} y_k(r) &= \sum_{l=1}^{L} h_k^{(l)}(r)x(r) + v_k(r) \\ &= h_k(r)x(r) + v_k(r) \end{aligned} \tag{1}$$

where subscript k denotes the antenna element number, l is the wave index, and $r \in \{1,2,\ldots,R\}$ is the snapshot-index. A total of L waves are assumed. The channel coefficient is denoted by $h_k^{(l)}(r)$, the transmitted symbol is $x(r)$, and the noise is $v_k(r)$.

At the handset the outputs of the antenna elements are combined as

$$z(r) = \sum_{k=1}^{K} y_k(r)w_k(r) \tag{2}$$

where $w_k(r)$ is the weight for the k-th element, as described in the sections below.

A. Equal Gain Combining

Knowing the combined channel and antenna response for each element,

$$h_k(r) = B_k(r)e^{j\gamma_k(r)} \tag{3}$$

allows to set the weights to have opposite phases and hence eliminate phase differences and maximize the sum amplitude, *i.e.*,

$$w_k(r) = \frac{e^{-j\gamma_k(r-d)}}{\sqrt{K}}. \tag{4}$$

These weights results in what is known as EGC diversity in the literature [34]. The factor $\sqrt{K}$ is introduced to preserve the noise power before and after the combiner, making comparisons easier. The estimation delay parameter d is discussed further in Section V. Assuming ideal conditions with $d = 0$, the power of the signal part in the combiner output is

$$|z(r)|^2 = \frac{|x(r)|^2}{K}\left|\sum_{k=1}^{K} B_k(r)\right|^2 \tag{5}$$

i.e., all the available power is captured. It is noted that the EGC approach does not assume any relation between the phases for different branches, and hence achieves the optimum result irrespective of the number incident waves and whether or not they are plane. Since the EGC approach only aligns the phases it does not take into account the signal to noise ratio (SNR) of the individual branches, as opposed to the maximum ratio combining (MRC) approach. However, the performance gain of MRC over EGC, in terms of the combiner SNR statistics, turns out to be rather small [34].

In order to use the EGC approach in practice, the channel phase for each antenna element must be estimated, *e.g.*, by using the reference signals mentioned in Section I. Typically the number of Rx branches must also equal the number of elements, K, which is costly in both hardware (HW) and power consumption. To avoid using multiple Rx branches, one might consider obtaining the complex coefficients for the different branches by switching a single Rx (or Tx), where the weights are then applied using phase shifters. However, this requires the phases to be essentially unchanged during the switching phase, which may be difficult ensure in many practical scenarios.

B. Beam Scanning

In the BS approach, knowledge of the antenna array is exploited. In the following, the amplitude and phase of the χ-polarization component of the k-th element response to a plane wave arriving at the angle pair $\rho = [\phi, \theta]$ is given by $A_k^{\chi}(\rho)$ and $\zeta_k^{\chi}(\rho)$, respectively, where the usual spherical coordinate system is assumed and χ stands for either of the orthogonal polarizations θ or ϕ.

For BS the weights are of the form

$$w_k(r) = \frac{e^{-j\zeta_k^{\chi}[\rho^*(r-d)]}}{\sqrt{K}} \tag{6}$$

where the $\sqrt{K}$ factor again eases comparisons and $d \geq 0$ is a delay variable. The optimum direction is found by searching for the maximum power using the signals received, *i.e.*,

$$\rho^*(r) = \arg\max_{\rho} |z(r;\rho)|^2 \tag{7}$$

where $z(r;\rho)$ is the array output when choosing ρ, defined by inserting $w_k(r) = e^{-j\zeta_k^{\chi}(\rho)}$ in (2). Ideally, using these weights corresponds to forming a beam in the direction given by ρ, as in the case of an ideal uniform linear array (ULA). It is noted that two sets of weights may be found, depending on the choice of polarization in (6), which should be selected according to the dominant property of each antenna element,

Published in *IEEE Transactions on Antennas and Propagation*, Vol. 70, No. 7, p. 5725–5735, July 2022. DOI: 10.1109/TAP.2022.3161567.

if any. In the following both choices are tested, where BS1 and BS2 refers to using the weights optimized using the phase of the θ- and ϕ-polarization, respectively. In general the scanning for maximum power may also include matching to the polarization at the Rx, which may differ from that of the Tx, due to the channel. This is not pursued in the current work, since all elements have the same polarization.

A main advantage of the BS approach is that it allows the use of only a single Rx branch, where the weighting of the element outputs is implemented via phase shifters in HW. The search for maximum weighted output power must be carried out in a training phase, *e.g.*, using reference signals, causing a time-overhead. Another major disadvantage of using phase shifters is the relatively large insertion loss, in the range 6–8 dB [35]. However, integrated solutions with low noise amplifiers (LNAs) and phase shifters offer noise figures in the range 3.5–5 dB [36], [37].

The channel coefficients in (1) may be expanded as

$$h_k^{(l)} = \alpha^{(l)} A_k(\rho^{(l)}) e^{j\zeta_k(\rho^{(l)})} \tag{8}$$

where $\alpha^{(l)}$ and $\rho^{(l)}$ denote the complex amplitude and direction of arrival (DOA) of the l-th wave, respectively. For simplicity, a single polarization is assumed. Inserting (8) into (1) and omitting the noise term, the received power is

$$|z(r;\rho)|^2 = \left| \frac{x(r)}{\sqrt{K}} \sum_{k=1}^{K} e^{-j\zeta_k(\rho)} \sum_{l=1}^{L} \alpha^{(l)} A_k(\rho^{(l)}) e^{j\zeta_k(\rho^{(l)})} \right|^2 \tag{9}$$

where the weights are assumed to be of the form in (6) with $d = 0$. If only a single plane wave is present, $L = 1$, choosing $\rho = \rho^{(1)}$ maximizes the power which is furthermore the same as that achieved with EGC. However, when $L > 1$ or if the incoming waves are not plane, it may not be possible to align the phases from all elements and the power achieved with BS will be less than that for EGC. A reduced power will also be obtained if the polarization of incoming waves do not match that used for the weight optimization.

IV. Array Coverage Efficiency

Proposed in [16], the coverage efficiency is a metric of how well an antenna provides high gain in different directions. Using the total scan pattern defined by the maximum achievable gain for each direction, the coverage efficiency is the area of the total scan pattern exceeding a given gain threshold, as a ratio to the full sphere area.

Fig. 4 shows the total scan pattern for the array used in this work, obtained using the measured radiation patterns and weights obtained with the BS approach, *i.e.*, using (6). For the evaluation it is assumed that the received field has unit power in both polarizations. The figure shows the result achieved with weights based on the θ-polarization. Using the ϕ-polarization for the weights results in a very similar plot.

The elements of the array are located along the top front of the mockup handset and hence beams can only effectively be formed in the front and back of the handset, corresponding to ϕ-angles of around 0° and 180°, whereas the gain is low in directions near the array ends, *i.e.*, near ϕ-angles of 90°

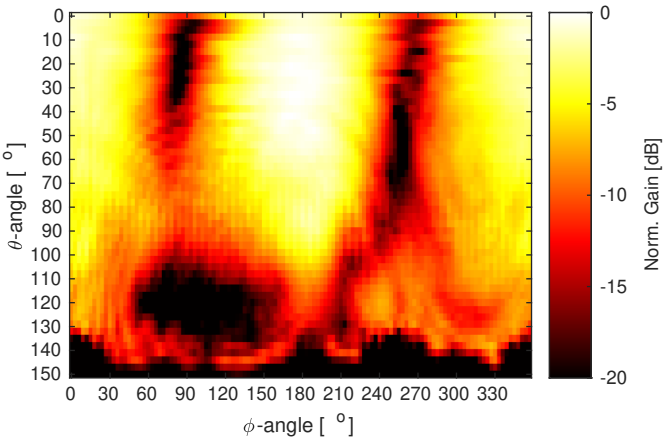

Fig. 4. Total scan pattern, normalized to maximum gain, for weights obtained from the θ-polarization component.

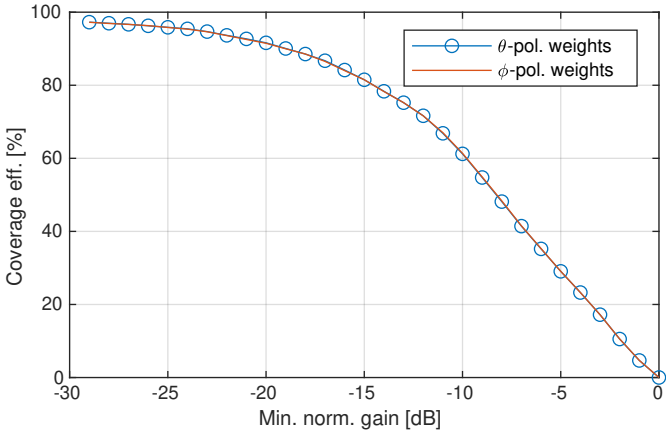

Fig. 5. Coverage efficiency for normalized gain patterns achieved with weights from both ϕ- and θ-polarization components.

and 270°. The handset was slanted to 60° both during the measurements in the corridor and in the anechoic room.

The coverage efficiency is shown in Fig. 5 with virtually identical results achieved when ϕ- and θ-polarized weights are used. The figure shows that more than about 80% of the directions have a gain of -15 dB below the peak value, or better. Higher gains can be achieved, but only at a percentage which is decreasing with the gain demand. The radiation patterns are only measured for $\theta \leq 150°$ and only these angles are considered when computing the gains. It is important to notice that the coverage efficiency is computed based on the radiation pattern measured in free space and thus does not take into account the influence of the user, which will depend on the specific person and how the person handles the mockup during the measurements.

V. Measurement Processing

The measurements described in Section II allow a novel evaluation of the EGC and BS combiners in a real propagation environment, including the practical influence a user has on the performance.The data obtained from the propagation measurements are represented as CIRs, denoted as $g_k^{\xi}(\tau, r)$, where

Published in *IEEE Transactions on Antennas and Propagation*, Vol. 70, No. 7, p. 5725–5735, July 2022. DOI: 10.1109/TAP.2022.3161567.

$k \in \{1,2,\ldots,K\}$ is the Rx antenna index, $r \in \{1,2,\ldots,R\}$ is the snapshot index, $\tau \in \{1,2,\ldots,T\}$ is the delay index, and ξ is the BS polarization given by the Tx index. $T = 500$ is the number of samples in delay. Although the combining described in Section III only considers narrow-band (NB) channels, the wide-band (WB) measurements are utilized in the analysis as described below. In the description, the polarization index ξ is omitted, since the steps are carried out independently for both polarizations.

In the processing it is important to take into account that noise inevitable will be present in the non-ideal measurements. To this end, the instantaneous noise and signal power are estimated from the WB data as

$$\tilde{P}_k(r) = \sum_{\tau=1}^{S} \frac{|g_k(\tau,r)|^2}{S} - S\tilde{\sigma}_k(r) \tag{10}$$

$$\tilde{\sigma}_k(r) = \sum_{\tau=S+1}^{T} \frac{|g_k(\tau,r)|^2}{T-S} \tag{11}$$

where the first $S = 100$ samples in delay are assumed to contain both noise and all the signal components, and the remaining $T - S$ samples only contain noise. The choice of $S = 100$ corresponds to a signal window of 250 ns. Both the signal power $\tilde{P}_k(r)$ and the noise power $\tilde{\sigma}_k(r)$ may vary with the snapshot index r, but are fixed during the individual snapshots. Defining the instantaneous SNR $\psi(r)$ as the average over the Rx branches,

$$\psi(r) = \frac{1}{K}\sum_{k=1}^{K} \frac{\tilde{P}_k(r)}{\tilde{\sigma}_k(r)} \tag{12}$$

the following analysis only includes snapshots with indices in the set $Q_r = \{r | \psi(r) \geq 15 \text{ dB};\ r \in \{1,2,\ldots,R\}\}$, *i.e.*, snapshots with an SNR of at least 15 dB.

With the purpose of obtaining as many channel samples as possible, the individual sub-channels comprising the WB channel are utilized. The samples are normalized as follows,

$$H_k(f,r) = \frac{G_k(f,r)}{\sqrt{\frac{\tilde{P}_k(r)}{\sharp Q_r}\sum_{r' \in Q_r} |G_k(f,r')|^2}} \tag{13}$$

where $G_k(f,r)$ is given by the discrete Fourier transform of the vector formed by the first S delay-indices of the snapshot, *i.e.*, $[g_k(1,r), g_k(2,r), \ldots, g_k(S,r)]$. Note that the set size $\sharp Q_r$ depends on the measurement since the instantaneous SNRs vary with the specific scenario. The samples in (13) are normalized by both the total snapshot power and the average power for each sub-channel, where the latter eliminates the gain differences due to the fixed Tx and Rx filters. The normalization with the total snapshot power ensures that it makes sense to concatenate data from different snapshots, which are obtained for different orientations of the handset in the environment. Note that despite the normalization, the NB channels are subject to fading and the power will vary among the sub-channels of the same snapshot, as well as for different snapshots.

For the subsequent processing the sub-channels with indices in the set $f \in \{1,2,\ldots,V,S,S-1,\ldots,S-V+1\}$ are used where $V = 8$, corresponding to selecting all sub-channel within the 3 dB bandwidth (BW) of the calibrated system response. Thus, for each snapshot $2V$ sub-channels are used and in total $\sharp Q_r \cdot 2V$ samples are available for processing when all snapshots with sufficient SNR are concatenated. The vector of concatenated samples is what is used for the following analysis, where it is noted that for each measurement the steps described above are carried out independently for Tx1 and Tx2, corresponding to the two polarizations. For each measurement, the EGC and BS weighting approaches are applied to each of the $\sharp Q_r \cdot 2V$ snapshots, using different parameters, and statistics of the resulting samples $|z(r')|^2$ are computed, where $r' \in \{1,2,\ldots,\sharp Q_r \cdot 2V\}$. Since the weighting vectors in (4) and (6) are scaled by $\sqrt{K}$, the total noise power is preserved. By also assuming normalized Tx power, $|x(r')| = 1$, changes in the statistics of $|z(r')|^2$ as a result of the combining methods is reflecting corresponding changes in the statistics of the observed SNR at the Rx.

TABLE I
DECIMATION OF MEASURED RADIATION PATTERN DATA.

Dec. fac. a	Angle step $a\Delta_\phi = a\Delta_\theta$	No. ϕ-angle N_ϕ	No. θ-angle M_θ	No. DOA $N_\phi M_\theta$
1	3°	120	51	6120
2	6°	60	26	1560
3	9°	40	17	680
5	15°	24	11	264
10	30°	12	6	72
15	45°	8	4	32
20	60°	6	3	18

In practice the search for maximum power in (7) for the BS approach is carried out using an exhaustive search in a grid defined by the measured antenna radiation patterns. The evaluated DOAs are given by all the possible combinations of angles defined by

$$\phi_n = na\Delta_\phi, \qquad n \in \{0,1,\ldots,N_a\} \tag{14}$$

$$\theta_m = ma\Delta_\theta, \qquad m \in \{0,1,\ldots,M_a\} \tag{15}$$

where $\Delta_\phi = \Delta_\theta = 3°$ are the angle sampling increments of the measured patterns, and $N_a = \lfloor 357°/(\Delta_\phi a)\rfloor$ and $M_a = \lfloor 150°/(\Delta_\theta a)\rfloor$. The integer $a \geq 1$ is the angle decimation factor introduced to allow analyzing the impact of varying the density of the measurement angle grid. Table I shows the considered values of a and the corresponding number of DOAs.

With the purpose of investigating the sensitivity of results to delays in the channel estimation, relevant for EGC, and for the time it takes to scan all directions, relevant for BS, a delay parameter was introduced in (4) and (6). The delay introduced is dT_s where $d \in \{0,1,2\}$ is the parameter and $T_s = 11.1$ ms is the snapshot time separation.

VI. RESULTS

As described above, each snapshot is evaluated and only included in the analysis if the SNR is minimum 15 dB. Since 1800 snapshots are obtained during each measurement, a maximum of 28,800 samples are available for analysis when all snapshots have a sufficient SNR. Table II gives an overview of the number of analyzed samples, as percentages of the

Published in *IEEE Transactions on Antennas and Propagation*, Vol. 70, No. 7, p. 5725–5735, July 2022. DOI: 10.1109/TAP.2022.3161567.

TABLE II
OVERVIEW OF THE NO OF SNAPSHOTS WITH AT LEAST 15 DB INSTANTANEOUS SNR AS PERCENTAGE OF THE MAXIMUM 28,800 IN EACH MEASUREMENT. MIN AND MAX VALUES ARE AMONG THE MEASUREMENTS OBTAINED AT EACH LOCATION.

		Min		Max	
Location	No. Meas.	Tx1	Tx2	Tx1	Tx2
L1	1	45%	6%	45%	6%
L2	4	63%	35%	74%	73%
L3	5	82%	83%	100%	100%
L4	6	100%	100%	100%	100%
L5	20	99%	100%	100%	100%
L6	6	100%	100%	100%	100%
L7	24	100%	100%	100%	100%
L8	6	100%	100%	100%	100%
L9	6	100%	100%	100%	100%
L10	6	100%	100%	100%	100%

maximum number for the different locations, L1, L2, ..., L10. The percentages are given as minimum and maximum values among the several measurements that were made at most of the locations. The table shows that most of the snapshots have SNRs above the threshold, except for L1/L2 particularly for Tx2. L1 is the location furthest away from the Tx and hence is expected to have the generally largest pathloss, and turns out to be near the maximum range of the measurement system in this setup.

Examples of the results obtained with the different combiner methods are shown in Fig. 6 for a measurement at location L5 for person no. 1. The curves show the resulting power levels versus the snapshot index, and are for the case of transmitting with Tx1. The figure shows results for only some of the snapshots. It is noticed that power levels vary considerably due to the user's rotation in the environment. The curve labeled 'Indv. (Rx4)' is the power received by a single array element, included for comparison. As expected, the power is fluctuating with deep fades of more than 30 dB, in some cases. The curves for EGC, BS1, and BS2 are relatively close and with generally less severe fading in addition to a significant gain over the single branch curve, due to the use of 7 elements.

For an easier comparison, Fig. 7 shows the cumulative distribution functions (CDFs) obtained for the same example measurement, where also a curve for a simulated Rayleigh channel has been included for reference. Note that the CDF for the case of using no combiner is obtained by concatenating data from all seven branches and hence more samples are available. It should also be noted that due to the rotation performed by the user holding the handset, the channel can be expected to be non-stationary, even though the power is normalized as described above. Therefore, the CDFs obtained are merely a tool for comparing the performance of the different combiners and may not fit those for specific channel models, such as Rayleigh or Ricean.

The curves in Fig. 7 for BS1 and BS2 are close to being identical, *i.e.*, the polarization used for scanning is unimportant. The curve for EGC is slightly better than those for the BS combiners, and the curves for BS1, BS2, EGC all have a steeper slope than both the reference curve and the curve for the individual elements, thus having more favorable statistics.

In order to condense the results and allow easier comparison

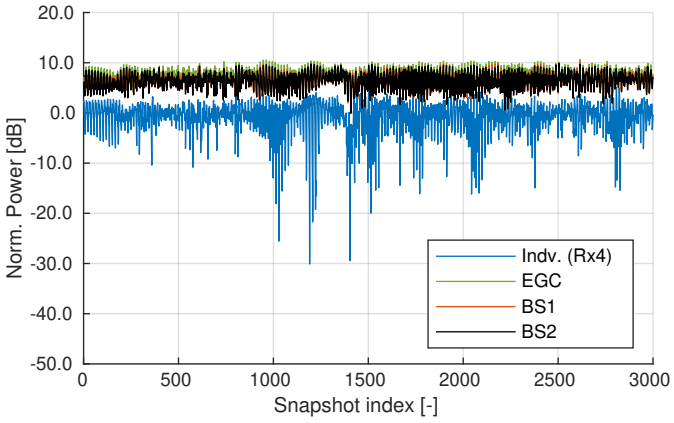

Fig. 6. The normalized power obtained with different combiners, and without combiner ('Indv. (Rx4)') for a measurement where Tx1 is used, and person no. 1 is at location L5. Note that the curves for EGC, BS1, BS2 are very close.

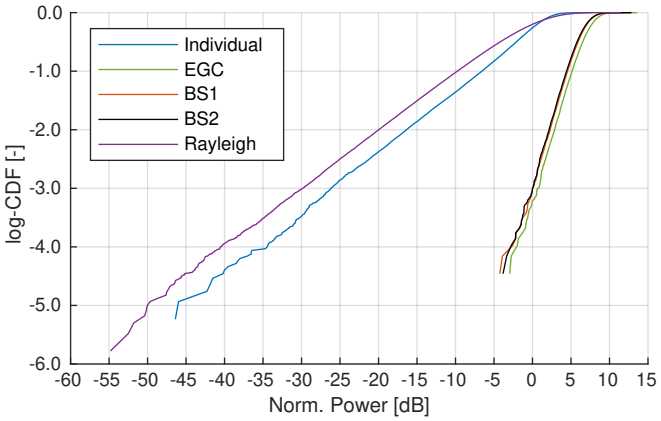

Fig. 7. The CDFs of the normalized power obtained with different combiners, and without combiner ('Individual') for a measurement where Tx1 is used, and person no. 1 is at location L5. Also results for a simulated 'Rayleigh' channel are shown.

of the results achieved with the different combiners for the different measurements, the following uses the 1st percentile of the power level after the combiner as a metric, denoted as the β-level. Using the 1st percentile is a compromise, where the empirical CDF curve is relatively stable and unaffected by individual samples while typically low enough to be part of the curve with an approximately constant slope.

A. *Repeated Measurements*

It is important to assess the variations in the chosen β-metric as a result of the non-ideal measurement system and uncontrolled changes in the environment. For this purpose the repeated measurements are utilized, where measurements are carried out in the same conditions. Although repeated, the snapshots are not expected to be acquired at exactly the same physical locations, and although the environment was kept static in the vicinity of the Tx and Rx, other parts may change, such as people moving in the background, *etc.*

Fig. 8 shows the statistics obtained from the repeated measurement with a single person at L5 and L7, and for

Published in *IEEE Transactions on Antennas and Propagation*, Vol. 70, No. 7, p. 5725–5735, July 2022. DOI: 10.1109/TAP.2022.3161567.

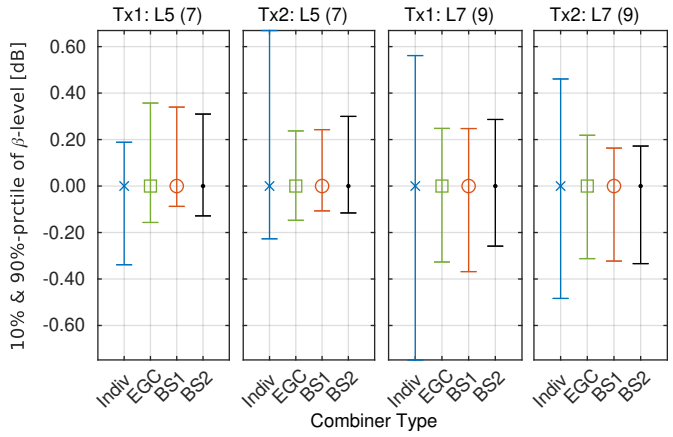

Fig. 8. Statistics of β-values for repeated measurements, where the median is subtracted in each case. 10th and 90th percentiles are shown as lower and upper line endpoints, respectively. The title of each sub-plot is of the form Ln (m), where m is the available number of measurements at location number n.

both Tx'es. Since the focus is on variations, the median is subtracted and the line bottom and top endpoints indicate the 10th and 90th percentile, respectively. From the figure, 80% of the repeated values fall within a range of about ± 0.7 dB around the median values.

B. Location Dependency

Although the snapshots are normalized with respect to power, as described above, the propagation scenarios for the measurement at different locations vary and may influence how the different combiners perform. With the purpose of investigating to what degree this is the case, Fig. 9 shows statistics of the β-values obtained at the different locations. All the measurements are included, both measurements with a person and in free space and any repetitions, and the 10th, 50th, and 90th percentiles are computed for each location.

In order to ease the comparisons, the percentiles for the results when no combiner is used ('Indiv' labels) are offset by the average difference between results for no combiner and those for EGC, BS1, BS2 (median values) for at each location. The offsets are 17.6 dB and 17.9 dB for the Tx1 and Tx2, respectively, and also represents the average improvement of the EGC and BS combiners over single-branch systems.

Using the BS approach is close to give the same results as EGC, where the median of the latter on average is about 0.6 dB higher than the median BS results. The median values varies within about 1.1–4 dB for Tx1 and 1.5–5.1 dB for Tx2 and thus some variation with the location is found. Clearly, the variations in the median values versus location for the different combiner types are correlated, where the LOS locations L7-10 seem more stable than the NLOS locations L1-6.

The influence that the user holding the handset has on the performance can be observed by comparing the median values to the similar mean values obtained from only the free space measurements, shown in Fig. 9 with '$\diamondsuit$' for each location-combiner combination. The largest differences are obtained for the case of no combiner, where values from about -1.2 dB to 2.1 dB are found for Tx1 and for Tx2 from about -1.3 dB to 3.6 dB. A positive difference indicates a higher channel gain in free space compared to the case with user. For EGC, BS1, and BS2 the differences are similar, with values from about -1.4 dB to 1 dB for Tx1, and from about -0.2 dB to 1.1 dB for Tx2. Thus, user presence can lead to both lower and higher median channel gain, depending on the location and suggesting that in some locations the benefits obtained from the scattering by the user outweighs the disadvantages caused by the user blocking incoming power. The gain difference is rather small as a mean over the locations, about 0.3 dB (0.6 dB) for Tx1 (Tx2) when no combiner is used, and for the EGC, BS1, BS2 combiners it is about 0.1 dB (0.3 dB) for Tx1 (Tx2).

C. Non-Ideal Channel State Information

The results presented above are all based on the assumption that ideal CSI is available at the Rx. In practice this will not be the case, and the combiner performance is expected to degrade. In this section, two aspects of non-ideality are considered.

The first aspect is delay in the acquisition of the CSI. It takes a certain amount of time to estimate the channel before the result can be utilized in the EGC combiner, and during this time the channel may have changed, leading to a sub-optimum result. For the BS combiner the Rx has to test a number of different beam directions before the best can be selected. This process takes time, in which the channel may change so that the chosen direction may become sub-optimum. By utilizing that the measurements contain realistic sequences of CSI, the following presents a novel investigation of the impact delayed CSI has on BF performance.

The second aspect of non-ideality considered is the number of directions which are tested in the BS approach, as described in Section V and Table I. Increasing the number of tested directions, and hence the grid-search density, allows a selection closer to the optimum direction. However, the number of tested directions is linked to the time used for the search, so that a higher number of directions increases the risk of channel changes during the search.

Fig. 10 shows results for Tx1 in subplots, one for each estimation delay, and with the number of BS directions considered along the x-axis. The top plot shows the mean of the β-values obtained for all the different measurements, while the bottom plot shows the standard deviation. Similarly, Fig. 11 shows the results obtained for Tx2. For reference, the 'Indiv' curves are the statistics obtained when no BF is used.

By increasing the number of tested directions in the BS from 18 to 6120, the mean β-value is overall increased by some 4 dB, which is largely independent on the polarization and assumed delay. As expected, most of the improvement is observed when going from 18 to 264 directions, corresponding to decreasing the angle step from 60° to 15°.

However, introducing a delay between determining the BF weights and actually using them is critical. Some 8 dB is lost in mean when a delay of 22 ms is assumed. A delay also increases the variation in the β-value observed among the measurements, for Tx1 (Tx2) from about 0.7 dB (0.5 dB) without delay to about 1.9 dB (2.1 dB) for a 22 ms delay. Further, the EGC approach has a higher variation relative to that of the BS approach.

Published in *IEEE Transactions on Antennas and Propagation*, Vol. 70, No. 7, p. 5725–5735, July 2022. DOI: 10.1109/TAP.2022.3161567.

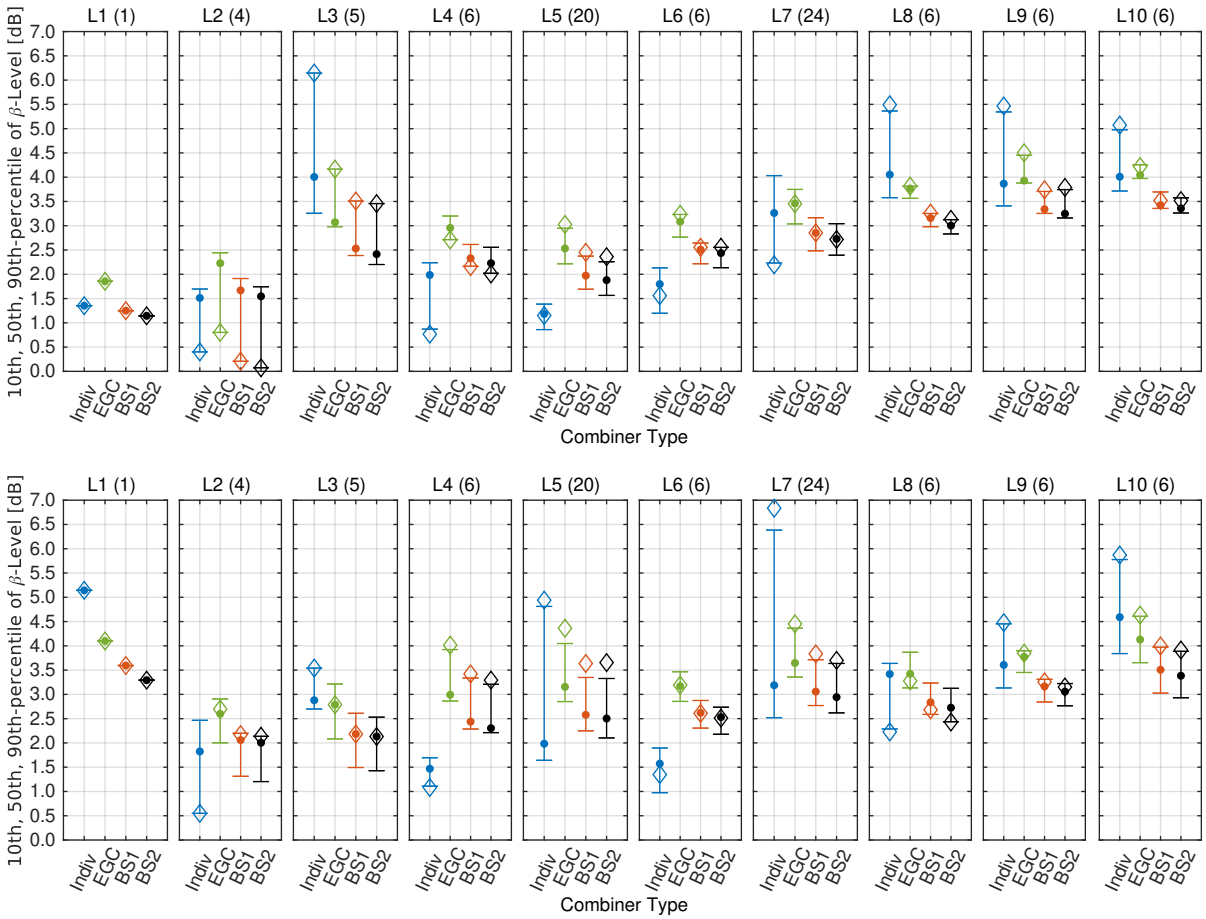

Fig. 9. 10th-, 50th-, 90th-percentile of the β-level for all measurements at the same location, shown as low, middle, and high points of bars, respectively. Diamonds ('◊') indicate median values for free space measurements. The title of each sub-plot is of the form Ln (m), where m is the available number of measurements at location number n. The top/bottom plot is for Tx1/Tx2, respectively. Note that values for 'Indiv' are added 17.6 dB and 17.9 dB, for Tx1 and Tx2, respectively.

VII. Conclusions

Using measurements at 21.5 GHz of the channel between a fixed transmitter and a 7-element mockup handset at different locations in a corridor, both in LOS and NLOS, the performance of different beamforming (BF) approaches were evaluated. The measurements involve several users of the mockup, allowing a novel investigation of BF performance including aspects of changes caused by the users, the location as well as impact of imperfect channel state information (CSI). The evaluation is based on the 1st percentile of the normalized power achieved with the BF as the channel changes due to user movement.

Assuming ideal knowledge of the CSI, the power with the beam scanning (BS) approach is only about 0.6 dB lower than the power achieved with the equal gain combining (EGC) approach, in average over all locations and users. Depending on the location the power may vary up to about 5 dB. On average, the BF gains are 17.6 dB and 17.9 dB, when transmitting using vertical and horizontal polarization, respectively.

Free space conditions may lead to higher or lower power compared to the median of cases both with and without a user, in the range of -1.3 dB to 3.6 dB, depending on location and polarization. In average over all locations, the free space power is 0.1 dB to 0.6 dB higher than the general case, depending on the combiner type and polarization.

For the BS approach, the scanning grid density impacts the performance which is also inferior to that of the EGC approach which does not assume single plane waves. On average, the power obtained for BS is within 1–2 dB of the EGC reference case, assuming a scanning grid step of 15° or smaller, with up to about 4 dB extra degradation if larger steps up to 60° are used.

In practical use ideal knowledge of the CSI cannot be assumed and the channel may change from the moment of the BF weights are determined to the moment they are applied. Using the measured data a mean degradation of some 8 dB was found for a 21 ms delay for the EGC and with a similar degradation for the BS approach, thus indicating that timely CSI is crucial to the performance.

Acknowledgments

This work was supported by the Danish National Advanced Technology Foundation project "Virtuoso."

Published in *IEEE Transactions on Antennas and Propagation*, Vol. 70, No. 7, p. 5725–5735, July 2022. DOI: 10.1109/TAP.2022.3161567.

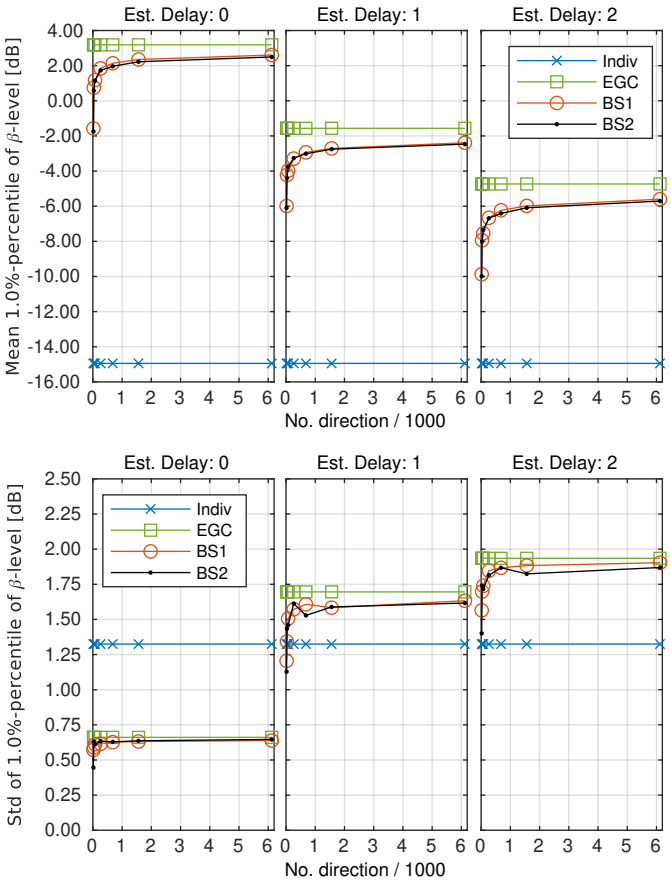

Fig. 10. The β-level for Tx1 shown as mean (top) and standard deviation (bottom) of all measurements obtained at different locations, both with and without a person holding the handset.

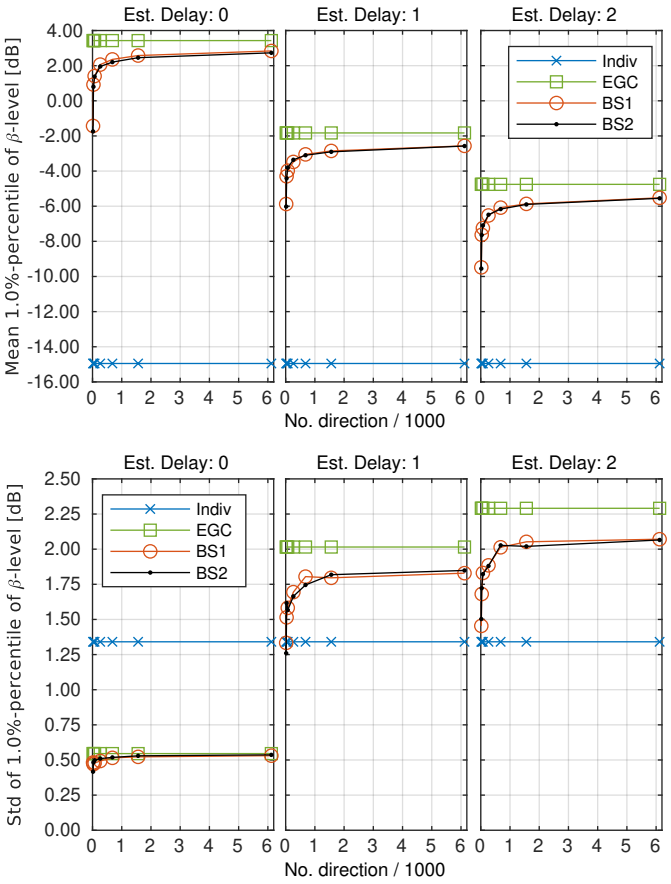

Fig. 11. The β-level for Tx2 shown as mean (top) and standard deviation (bottom) of all measurements obtained at different locations, both with and without a person holding the handset.

REFERENCES

[1] Q. C. Li, H. Niu, A. T. Papathanassiou, and G. Wu, "5G network capacity: Key elements and technologies," *IEEE Veh. Technol. Mag.*, vol. 9, no. 1, pp. 71–78, 2014.

[2] "3rd generation partnership project; technical specification group radio access network; NR; user equipment (UE) radio transmission and reception; part 2: Range 2 standalone (3GPP TS 38.101-2 V16.5.0 (2020-09))," http://www.etsi.org/standards-search.

[3] Z. Pi and F. Khan, "An introduction to millimeter-wave mobile broadband systems," *IEEE Commun. Mag.*, vol. 49, no. 6, pp. 101–107, 2011.

[4] J. N. Murdock, E. Ben-Dor, Y. Qiao, J. I. Tamir, and T. S. Rappaport, "A 38 GHz cellular outage study for an urban outdoor campus environment," in *2012 IEEE Wireless Communications and Networking Conf. (WCNC)*, 2012, pp. 3085–3090.

[5] T. S. Rappaport, F. Gutierrez, E. Ben-Dor, J. N. Murdock, Y. Qiao, and J. I. Tamir, "Broadband millimeter-wave propagation measurements and models using adaptive-beam antennas for outdoor urban cellular communications," *IEEE Trans. Antennas Propag.*, vol. 61, no. 4, pp. 1850–1859, 2013.

[6] T. S. Rappaport, G. R. MacCartney, M. K. Samimi, and S. Sun, "Wideband millimeter-wave propagation measurements and channel models for future wireless communication system design," *IEEE Trans. Commun.*, vol. 63, no. 9, pp. 3029–3056, Sep. 2015.

[7] H. Zhao, R. Mayzus, S. Sun, M. Samimi, J. K. Schulz, Y. Azar, K. Wang, G. N. Wong, F. Gutierrez, and T. S. Rappaport, "28 GHz millimeter wave cellular communication measurements for reflection and penetration loss in and around buildings in new york city," in *2013 IEEE Int. Conf. Communications (ICC)*, 2013, pp. 5163–5167.

[8] P. Ökvist, H. Asplund, A. Simonsson, B. Halvarsson, J. Medbo, and N. Seifi, "15 GHz propagation properties assessed with 5G radio access prototype," in *2015 IEEE 26th Annu. Int. Symp. Personal, Indoor, and Mobile Radio Communications (PIMRC)*, 2015, pp. 2220–2224.

[9] J. Lee, K. Kim, M. Kim, and J. Park, "Multipath characteristics of outdoor-to-indoor propagation based on 32-GHz measurements," in *2020 14th European Conf. Antennas and Propagation (EuCAP)*, March 2020, pp. 1–5.

[10] J. Lee, K. Kim, M. Kim, J. Park, Y. K. Yoon, and Y. J. Chong, "Measurement-based millimeter-wave angular and delay dispersion characteristics of outdoor-to-indoor propagation for 5G millimeter-wave systems," *IEEE Access*, vol. 7, pp. 150 492–150 504, 2019.

[11] P. Zhang, B. Yang, C. Yi, H. Wang, and X. You, "Measurement-based 5G millimeter-wave propagation characterization in vegetated suburban macrocell environments," *IEEE Trans. Antennas Propag.*, vol. 68, no. 7, pp. 5556–5567, July 2020.

[12] J. Park, J. Lee, K. Kim, M. Kim, H. Kwon, and K. C. Lee, "Wide-sense stationarity of millimeter wave expressway channels based on 28 GHz measurements," in *2019 IEEE 90th Vehicular Technology Conf. (VTC2019-Fall)*, Sep. 2019, pp. 1–5.

[13] F. Erden, O. Ozdemir, and I. Guvenc, "28 GHz mmwave channel measurements and modeling in a library environment," in *2020 IEEE Radio and Wireless Symp. (RWS)*, Jan 2020, pp. 52–55.

[14] A. A. Dos Anjos, T. R. R. Marins, C. R. Nogueira Da Silva, V. M. Rodrigo Peñarrocha, L. Rubio, J. Reig, R. A. A. De Souza, and M. D. Yacoub, "Higher order statistics in a mmwave propagation environment," *IEEE Access*, vol. 7, pp. 103 876–103 892, 2019.

[15] W. Roh, J. Seol, J. Park, B. Lee, J. Lee, Y. Kim, J. Cho, K. Cheun, and F. Aryanfar, "Millimeter-wave beamforming as an enabling technology for 5G cellular communications: theoretical feasibility and prototype results," *IEEE Commun. Mag.*, vol. 52, no. 2, pp. 106–113, 2014.

[16] J. Helander, K. Zhao, Z. Ying, and D. Sjöberg, "Performance analysis of millimeter-wave phased array antennas in cellular handsets," *IEEE Antennas Wireless Propag. Lett.*, vol. 15, pp. 504–507, 2016.

[17] K. Zhao, J. Helander, D. Sjöberg, S. He, T. Bolin, and Z. Ying, "User body effect on phased array in user equipment for the 5G mmwave communication system," *IEEE Antennas Wireless Propag. Lett.*, vol. 16, pp. 864–867, 2017.

Published in *IEEE Transactions on Antennas and Propagation*, Vol. 70, No. 7, p. 5725–5735, July 2022. DOI: 10.1109/TAP.2022.3161567.

[18] "3rd generation partnership project; technical specification group radio access network; NR; physical channels and modulation (V16.7.0 (2021-09))," http://www.etsi.org/standards-search.
[19] M. Giordani, M. Polese, A. Roy, D. Castor, and M. Zorzi, "A tutorial on beam management for 3GPP NR at mmwave frequencies," *IEEE Commun. Surveys Tutor.*, vol. 21, no. 1, pp. 173–196, 2019.
[20] "3rd generation partnership project; technical specification group radio access network; NR; physical channels and modulation (3GPP TS 38.211 V16.3.0 (2020-09))," http://www.etsi.org/standards-search.
[21] M. Giordani, M. Polese, A. Roy, D. Castor, and M. Zorzi, "Standalone and non-standalone beam management for 3GPP NR at mmwaves," *IEEE Commun. Mag.*, vol. 57, no. 4, pp. 123–129, 2019.
[22] K. Zhao, O. Zander, T. Bolin, Z. Ying, S. Zhang, and G. F. Pedersen, "Integration and evaluation of antenna systems for 5G mmwave mobile device," in *2019 IEEE Int. Symp. Antennas and Propagation and USNC-URSI Radio Science Meeting*, July 2019, pp. 1075–1076.
[23] J. Zhang, K. Zhao, L. Wang, S. Zhang, and G. F. Pedersen, "Dual-polarized phased array with end-fire radiation for 5G handset applications," *IEEE Trans. Antennas Propag.*, vol. 68, no. 4, pp. 3277–3282, 2020.
[24] S. S. Kim, S. H. Kim, J. H. Bae, and Y. Joong Yoon, "Series chained patch phased array antenna for mmwave 5G mobile in metal bezel design," in *2019 IEEE Int. Symp. Antennas and Propagation and USNC-URSI Radio Science Meeting*, July 2019, pp. 279–280.
[25] J. Park, S. Y. Lee, Y. Kim, J. Lee, and W. Hong, "Hybrid antenna module concept for 28 GHz 5G beamsteering cellular devices," in *2018 IEEE MTT-S Int. Microwave Workshop Series on 5G Hardware and System Technologies (IMWS-5G)*, 2018, pp. 1–3.
[26] W. Hong, K. Baek, Y. Lee, Y. Kim, and S. Ko, "Study and prototyping of practically large-scale mmwave antenna systems for 5G cellular devices," *IEEE Commun. Mag.*, vol. 52, no. 9, pp. 63–69, 2014.
[27] J. Lee, M. Kim, K. Kim, and J. Park, "Measurement-based beam mis-alignment analysis of millimeter-wave directional beamforming in large indoor environments," in *12th European Conf. Antennas and Propagation (EuCAP 2018)*, April 2018, pp. 1–5.
[28] K. Heimann, J. Tiemann, D. Yolchyan, and C. Wietfeld, "Experimental 5G mmwave beam tracking testbed for evaluation of vehicular communications," in *2019 IEEE 2nd 5G World Forum (5GWF)*, 2019, pp. 382–387.
[29] K. Zhao, C. Gustafson, Q. Liao, S. Zhang, T. Bolin, Z. Ying, and S. He, "Channel characteristics and user body effects in an outdoor urban scenario at 15 and 28 GHz," *IEEE Trans. Antennas Propag.*, vol. 65, no. 12, pp. 6534–6548, Dec 2017.
[30] J. Hejselbæk, J. Ø. Nielsen, W. Fan, and G. F. Pedersen, "Measured 21.5 GHz indoor channels with user-held handset antenna array," *IEEE Trans. Antennas Propag.*, vol. 65, no. 12, pp. 6574–6583, Dec 2017.
[31] J. Ø. Nielsen, W. Fan, P. C. F. Eggers, and G. F. Pedersen, "A channel sounder for massive MIMO and MmWave channels," *IEEE Commun. Mag.*, vol. 56, no. 12, pp. 67–73, December 2018.
[32] Y. Wang, J. Li, L. Huang, Y. Jing, A. Georgakopoulos, and P. Demestichas, "5G mobile: Spectrum broadening to higher-frequency bands to support high data rates," *IEEE Veh. Technol. Mag.,* vol. 9, no. 3, pp. 39–46, 2014.
[33] N. Ojaroudiparchin, M. Shen, S. Zhang, and G. Pedersen, "A switchable 3D-coverage phased array antenna package for 5G mobile terminals," *IEEE Antennas Wireless Propag. Lett.*, vol. 15, pp. 1747 – 1750, Feb. 2016.
[34] R. Vaughan and J. B. Andersen, *Channels, propagation and antennas for mobile communications*. London, United Kingdom: The Institution of Electrical Engineers, 2003.
[35] Arralis, "Product datasheet, Ka band MMIC variable phase shifter, 17-21 GHz, LE-Ka1360303," Available at https://arralis.com (accessed 11-19-2020).
[36] "Anokiwave intelligent gain block Ka-band silicon IC AWMF-0143," www.anokiwave.com.
[37] "Mixcomm summit2629™ 5G 28GHz beamforming front end IC," www.mixcomm.com.

Jesper Ødum Nielsen received his master's degree in electronics engineering in 1994 and a PhD degree in 1997, both from Aalborg University, Denmark. He is currently employed at Department of Electronic Systems at Aalborg University, Denmark, in the Antennas, Propagation and Millimeter-wave Systems section. His main areas of interests are experimental investigation of the mobile radio channel and the influence mobile device users have on the channel. Among other things, he has been involved in Massive MIMO and mm-wave channel sounding and modeling, as well as measurements using live LTE networks. In addition he has been working with radio performance evaluation, including over the air testing of active wireless devices.

Gert Frølund Pedersen (Member, IEEE) was born in 1965. He received the B.Sc.E.E (Hons.) degree in electrical engineering from the College of Technology in Dublin, Dublin Institute of Technology, Dublin, Ireland, in 1991, and the M.Sc.E.E. and Ph.D. degrees from Aalborg University, Aalborg, Denmark, in 1993 and 2003, respectively. Since 1993, he has been with Aalborg University, where he is currently a Full Professor heading the Antennas, Propagation, and Millimeter-Wave Systems LAB with 35 researchers. He is also the Head of the Doctoral School on Wireless Communication with some 40 Ph.D. students enrolled. He has published more than 500 peer-reviewed articles, six books, and holds over 50 patents. He has also worked as a Consultant for developments of more than 100 antennas for mobile terminals, including the first internal antenna for mobile phones in 1994 with lowest SAR, the first internal triple-band antenna in 1998 with low SAR and high TRP and TIS, and lately various multiantenna systems rated as the most efficient on the market. He has worked most of the time with joint university and industry projects and have received more than 30 M€ in direct research funding. He is also the Project Leader of the MARSS project with a total budget of over 8 M€ investigating antenna systems for Nano satellite systems. He has been one of the pioneers in establishing over-the-air measurement systems. The measurement technique is now well established for mobile terminals with single antennas. He was chairing the various COST groups with liaison to 3GPP and CTIA for over-the-air test of MIMO terminals. He is also involved in MIMO OTA measurement. His research interests include radio communication for moving terminals especially small antennas, antenna systems, propagation, and biological effects.

Published in *IEEE Transactions on Antennas and Propagation*, Vol. 70, No. 7, p. 5725–5735, July 2022. DOI: 10.1109/TAP.2022.3161567.